Journal of Chromatography A, 1218 (2011) 5187–5194

Contents lists available at ScienceDirect

Journal of Chromatography A

journal homepage: www.elsevier.com/locate/chroma

Morphological analysis of physically reconstructed capillary hybrid silica monoliths and correlation with separation efficiency

Stefan Bruns[a], Takeshi Hara[b], Bernd M. Smarsly[b], Ulrich Tallarek[a,*]

[a] Department of Chemistry, Philipps-Universität Marburg, Hans Meerwein Strasse, 35032 Marburg, Germany
[b] Institute of Physical Chemistry, Justus-Liebig-Universität Giessen, Heinrich-Buff-Ring 58, 35392 Giessen, Germany

ARTICLE INFO

Article history:
Received 21 March 2011
Received in revised form 23 May 2011
Accepted 24 May 2011
Available online 1 June 2011

Keywords:
Hybrid silica monoliths
Physical reconstruction
Morphological analysis
Chord length distribution
Radial heterogeneity
Eddy dispersion

ABSTRACT

We report an experimental study on the structural (especially radial) heterogeneity of eleven 100 μm i.d. capillary tetramethoxysilane–methyltrimethoxysilane hybrid silica monoliths with different pore and skeleton sizes, which were imaged by an optimized confocal laser scanning microscopy method. This method allows the optical sectioning of the monoliths, which is a prerequisite for quantitative morphological image analysis. Both radial porosity profiles and chord length distributions were calculated in the macropore domain for each column from at least 100 complete cross-sectional views along the column axis. The statistical approach visualized radial heterogeneities on different length scales in the monolithic structures. Chord length distributions followed a simplified *k*-gamma function, and a structural parameter obtained from this function is introduced to provide a scalar measure of column heterogeneity. It enables the comparison of monoliths with different pore sizes and helps to establish correlations between the microscopic properties of a column, eddy dispersion, and its separation efficiency.

1. Introduction

Monolithic stationary phases were developed and introduced in HPLC as an alternative to particulate fixed-beds for potentially faster and more efficient separations [1–4]. In the hierarchically structured pore space of monoliths the macropores enable convective transport, whereas the mesoporous (and often also microporous) skeletons provide a large surface area accessible by diffusion. The morphology of many organic polymer monoliths resembles that of microglobular aggregates [5–7], typically with a broad pore size distribution, whereas silica monoliths show a more fractal morphology, with discrete sets of intraskeleton mesopores and interskeleton macropores [8]. The synthesis of silica monoliths for chromatography, introduced by Nakanishi and co-workers [9–14], allows modifying macropore size and skeleton thickness independently from another. The hierarchical pore morphology of silica monoliths results from their two-step preparation, i.e., a sol–gel mechanism overlapped with a spinodal phase transition as the first step (determining the domain size and macropore diameter), followed by a solvent exchange, which leaches out the silica skeleton to create the intraskeleton mesopore space.

Although the following characteristics can be modulated by the preparation protocols, typical silica monoliths have shown to offer high sample capacity per unit adsorbent volume [15,16], a permeability comparable to that of columns packed with 11 μm particles [16,17], and an efficiency equivalent to that of 2–3 μm particulate columns [18,19]. As a consequence, silica monoliths have a much lower separation impedance than either 5 or 3.5 μm particulate packings [20]. When 5 μm particles were the standard material for analytical HPLC columns, the monolithic supports appeared as a breakthrough development. However, it was recognized early that structural features inherent to the fabrication process limit the efficiency of silica monoliths. These structural features concern [1] (i) the large size distribution, random spatial distribution, and variable geometry of the interskeleton macropores; (ii) the size of the throughpores (N.B. The recent trend towards finer, particularly sub-2 μm, particles [21] realizes a smaller throughpore size at an essentially unchanged morphology of the particulate bed, whereas a comparable decrease in the domain size of silica monoliths has not been achieved yet.); and (iii) the macroscopic radial heterogeneity of cylindrical monolithic columns. The formation of gaps between monolith skeleton and column wall is supposed to result from the uneven character of the mechanical stress that is experienced by the monolith–wall interface during the sol–gel step of the synthesis when the silica skeleton shrinks back from the confining wall. This is a well-known problem, particularly for the rigid, but brittle silica monoliths prepared from pure tetramethoxysilane (TMOS) [1].

* Corresponding author. Tel.: +49 6421 28 25727; fax: +49 6421 28 27065.
E-mail address: tallarek@staff.uni-marburg.de (U. Tallarek).
URL: http://www.uni-marburg.de/fb15/ag-tallarek (U. Tallarek).

0021-9673/$ – see front matter © 2011 Elsevier B.V. All rights reserved.
doi:10.1016/j.chroma.2011.05.090

For particle-packed columns radial heterogeneities of different origin (depending on the particle characteristics, packing process, and column-to-particle diameter ratio) are well-known to contribute strongly to eddy dispersion through local fluctuations of the external porosity, permeability, and retention factors [22–28]. In the case of analytical [29] and semi-preparative [30] silica monolithic columns wall effects were shown to substantially affect the average cross-sectional plate height, and they have also been documented for monoliths in capillary format [31]. Therefore, the key to improving the separation efficiency of silica monoliths is a (primarily radially) more homogeneous macropore morphology. To resolve this issue for monoliths from capillary to preparative column formats and in each case distinguish between the individual contributions to eddy dispersion, from the macropore level up to the column scale, experimental as well as advanced simulation approaches are required that allow us to study eddy dispersion within the real morphology and on the inherent time and length scales behind these contributions.

We recently presented a fast, non-destructive, and quantitative confocal laser scanning microscopy (CLSM) method composed of column pretreatment, image acquisition, image processing, and statistical analysis of the image data to characterize the morphology of monoliths and particle-packed beds, exemplarily shown for a Chromolith CapRod column [32] and a 100 μm i.d. capillary packed with 2.6 μm Kinetex core–shell particles [33]. The method is generally applicable to silica-based particulate or monolithic columns in capillary format and can be used to visualize stationary phase structure. The approach yields a multitude of longitudinal and cross-sectional images in a short time and allows the fast scanning along large segments of a capillary column for heterogeneities in macropore morphology. Individual contributions to eddy dispersion, e.g., due to wall effects, can thus quickly be identified, enabling the optimization of silica monolith preparation for more efficient HPLC columns. Statistical analysis of the CLSM images yielded quantifiable morphological information in the form of chord length distributions for the macropore space and the skeleton. The data are comparable to those obtained by TEM image analysis [34], but easier to access, and describe the monolith's macropore morphology accurately and comprehensively, providing a clear advantage over estimates of the average domain size from SEM images.

This approach [32] has already been used to resolve hydrodynamic flow and transport in the reconstructed bulk macroporous domain of a 100 μm i.d. capillary silica monolith by direct numerical simulations on a supercomputing platform [35,36]. Excellent agreement was observed between experimental and simulated Darcy permeabilities. The flow field was analyzed in detail, including longitudinal and transverse velocity distributions, the occurrence of negative longitudinal velocities, as well as the beginning transition to the viscous-inertial flow regime [35]. Further, the pore scale (microscopic) insight provided by the simulations into the length scales on which eddy dispersion operates in the relatively homogeneous core region of the capillary silica monolith was complemented by conventional column scale (macroscopic) chromatographic plate height analysis, providing a comparison that quantified the severe efficiency loss due to the (CLSM-visualized) wall gaps and the associated transcolumn contribution to eddy dispersion [36]. These findings demonstrated that the heterogeneity of the bulk macropore space is much smaller than currently believed, and that the excellent performance of the bulk silica monolith is obscured in chromatographic practice by a special wall effect related to irregular voids within a layer of up to ~15 μm thickness at the capillary wall. Elimination of discrete voids at the capillary wall should therefore get priority in silica monolith preparation, as this measure promises much improved separation efficiencies [37].

In the current work, we use the CLSM-based approach [32] to investigate and compare the morphology of improved capillary hybrid silica monoliths [38]. For capillary silica monoliths with 100 μm i.d. and larger prepared from TMOS, serious wall defects (as a result of shrinkage during the sol–gel step of the synthesis) have been observed in SEM images [31]. Feeding methyltrimethoxysilane (MTMS) to the sol reduces the occurrence of such critical void regions and enabled the preparation of capillary hybrid silica monoliths of larger diameters [39,40] (see also pp. 109–110 in [1]). The incorporation of methyl groups into the silicate structure hinders the condensation of hydroxyl groups and therefore reduces the shrinkage. The structure of these hybrid monoliths is less brittle and more flexible, and it thus better compensates the physical stress during shrinkage [39]. We focus on an analysis of the physically reconstructed morphology to characterize the radial heterogeneity and local density fluctuations in 100 μm i.d. capillary hybrid silica monoliths.

2. Experimental

2.1. Chemicals and materials

Eleven capillary monoliths in 100 μm i.d. cylindrical fused-silica capillaries were employed for this study. They were prepared as hybrid silica columns with an additional MTMS-content of 15% following the procedures described by Hara et al. [38] (cf. Section 2.2 and Table 1 in [38]). In the following discussion the observed variations in chromatographic separation efficiency are explained by monolith morphology. Columns which showed chromatographic band broadening dominated by their macropore size (transchannel dispersion) according to our analysis are referred to as Hybrid Columns A1–A7, whereas columns dominated by radial heterogeneity and the associated transcolumn dispersion are referred to as Hybrid Columns B1–B4. The analyzed monoliths had an unmodified bare-silica surface, except for Hybrid Column A2, which had a C18-modified surface.

3-Carboxy-6-chloro-7-hydroxycoumarin (dye V450) was purchased from Endotherm Life Science Molecules (Saarbrücken, Germany), while 3-aminopropyltriethoxysilane came from Alfa Aesar GmbH (Karlsruhe, Germany). Glycerol, HPLC grade acetonitrile, methanol, ethanol, dimethylsulfoxide (DMSO), and dimethylformamide (DMF) were supplied by Sigma–Aldrich Chemie GmbH (Taufkirchen, Germany), and a Milli-Q gradient water purification system (Millipore, Bedford, MA, USA) was used to provide HPLC grade water.

2.2. Chromatographic separation efficiency

The HPLC configuration assembled for the chromatographic evaluation of 25–30 cm long, 100 μm i.d. capillary monoliths consisted of a K-2501 spectro-photometer (Knauer, Berlin, Germany) and an L-7100 pump (Hitachi, Tokyo, Japan) with split injection/flow mode using a Rheodyne 7125 analytical injector (Rheodyne, Cotati, CA, USA). A 30 μm i.d. fused-silica capillary was utilized as UV detection cell as well as connection from the monolith column's outlet to the detection window where the polyimide coating had been removed. This distance was fixed at 3.4 cm. The split ratio during the chromatographic measurements was controlled at $\sim 10^{-3}$, as described previously [31]. Chromatographic data were processed with Hitachi D-7000 HPLC System Manager (HSM) software. All plate heights were calculated under kinetic conditions for unretained thiourea in methanol/water 80/20 (v/v) at 30 °C and an average flow velocity of 1.0 mm/s through the monoliths. The detection wavelength was set to 210 nm.

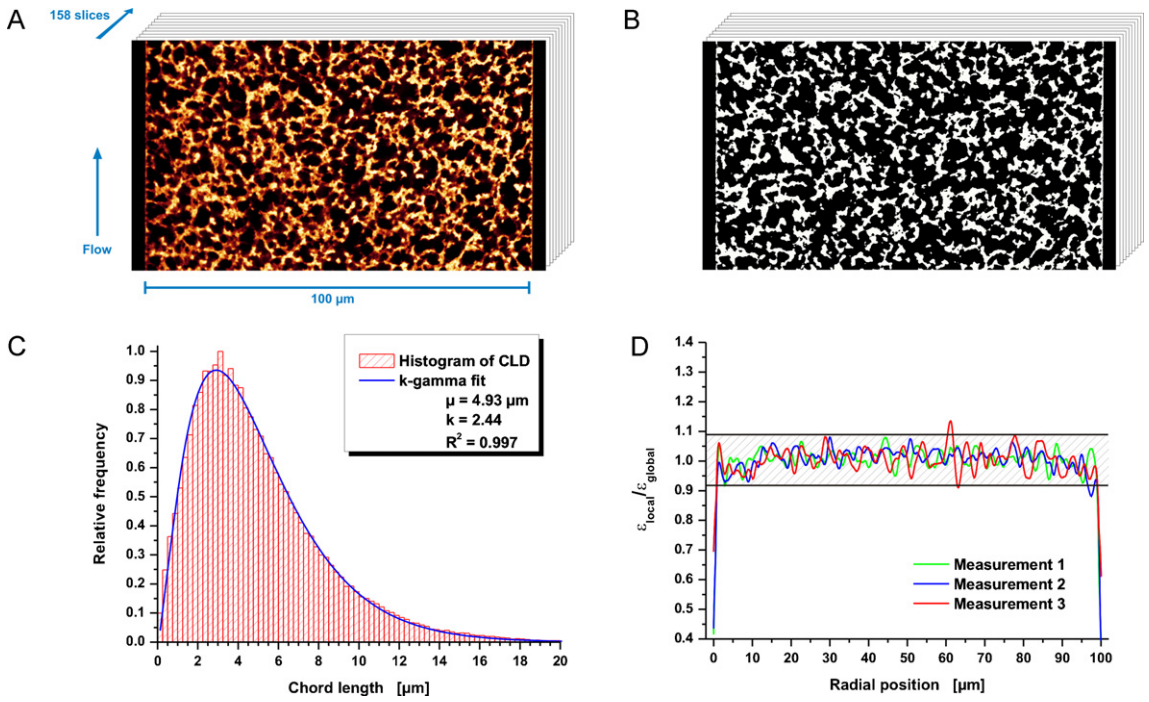

Fig. 1. Exemplary image from the second measurement of Hybrid Column A4 (A) and the segmentation result (B). 158 slices form the image stack that was used to obtain a histogram from 1×10^6 chord lengths. The histogram was fitted with a normalized *k*-gamma distribution (C). Normalized radial porosity profiles calculated for a step size of 30 nm smoothed with a 1 µm moving window for three image stacks obtained at different times and positions in the detection window's volume of Hybrid Column A4 (D). The shading designates an area of ±1 standard deviation around the global mean porosity.

2.3. Image acquisition

Prior to imaging by CLSM the silanol groups at the surface of the mesoporous monolith skeleton were labeled with a succinimidyl ester of dye V450, as described previously [32,33]. Each monolithic column was flushed with 100 µL of 3-aminopropyltriethoxysilane solution (0.1 M in ethanol) at 0.1 µL/min and 70 °C overnight. After cleaning with 500 µL of ethanol at 0.5 µL/min, 100 µL of V450-succinimidyl ester solution at 0.25 µL/min were introduced to bind V450 covalently to the monolith's surface. For bare-silica columns a dye concentration of 0.2 mg/mL DMF was found to yield high quality images consistently, whereas the decreased amount of binding sites in the C18-column was accounted for by increasing the dye concentration to 5 mg/mL.

All images were acquired on a TCS SP5 confocal microscopy system equipped with a HCX PL APO 63×/1.3 GLYC CORR CS (21°) glycerol immersion objective lens from Leica Microsystems (Wetzlar, Germany) by focusing into a capillary segment where the polyimide coating was removed with a drop of warm sulfuric acid. The column itself was filled with glycerol/DMSO/water 70/19/11 (v/v/v) and fixed on a microscope slide in an embedding pool of the same solvent mixture. For optimal refractive index matching this mixture was further calibrated with an AR200 digital refractometer (Reichert Analytical Instruments, Depew, NY, USA) to match the refractive index of the fused-silica capillary wall ($n_D = 1.4582$ [41]). The glycerol/DMSO/water mixture was also used as immersion medium for the microscope lens. A "type 0" cover slip (Gerhard Menzel GmbH, Braunschweig, Germany) was selected to separate embedding and immersion liquid minimizing spherical aberrations [33].

Excitation of dye V450 was realized with a 405 nm diode laser setting the pinhole of the microscope to 0.5 AU. Fluorescence emission was detected in the interval of 440–455 nm. Stacks of 100–200 8-bit grayscale images of 4096 × 2048 pixels were recorded from the column centre along the axis of the monolithic capillaries covering their whole diameter (see Fig. 1A). Pixel and step size were chosen as to remain below the Nyquist sampling criterion with 30 nm and 126 nm, respectively.

2.4. Image processing and analysis

Images were corrected for any z-drop by fitting a second-order exponential decay to the acquired image stack's intensity distribution along the dimension of the optical axis. Subsequently, Huygens maximum likelihood iterative deconvolution (Scientific Volume Imaging, Hilversum, The Netherlands) was applied for image restoration using an automated background estimate of the deconvolution software ("*in/near object*"-*estimate*) and a signal-to-noise ratio of 15. For image segmentation a copy of the acquired image stack was blurred with a Gaussian kernel and then subtracted from the deconvolved original [42]. Two hundred sigma were chosen as kernel size; a value that is large compared with image features and small compared with background variations [32]. This step was applied twice and any non-zero pixel was considered to be part of the monolithic skeleton (Fig. 1B). The image stack's faces that showed a continuing monolithic structure were cropped by 600 nm to avoid regions of poor restoration, resulting in reconstructions of the monolithic structures with macropore porosities between 0.68 and 0.72.

Image analysis was performed using custom software written with Visual Studio C# 2008 (Microsoft Corporation, Redmond, WA, USA) on at least hundred images for each column. The images were rotated to have the column walls aligned with the y-dimension of the image. Left and right column walls were defined as first and last y-column, respectively, in the image with a porosity of less than 0.98. Porosity profiles were then realized by binning pixel columns according to their minimal distance from the column wall and calculating the ratio between the amount of pixels assigned to the monolithic skeleton and the total amount of pixels in this bin.

Chord length distributions in the macropore space were calculated from random points generated in the background of the images for 32 angularly equispaced vector directions as described

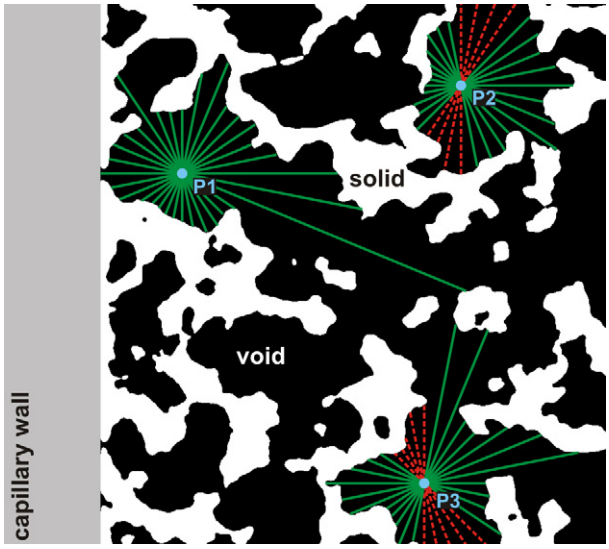

Fig. 2. Generation of a chord length distribution. Random points P1 to P*n* are generated in the void space of a reconstructed monolith and the linear skeleton-to-skeleton distance is determined for 16 equispaced directions (green lines). If a chord reaches out of the image boundaries it is rejected (red dashed lines), whereas chords touching the capillary wall are included. (For interpretation of the references to color in this figure legend, the reader is referred to the web version of the article.)

in [32–34]. Resulting chords describe a straight distance between two encounters with the monolith skeleton for 16 spatial directions. Chords that projected out of the image were discarded. Global statistics for the chord length distributions were collected from at least 4×10^5 chords randomly distributed over the image stack using the Levenberg–Marquardt algorithm [43] to fit a scaled *k*-gamma function, while prior binning of the seed points by their radial position in the column was used to calculate radial pore size profiles. New seeds were generated until at least 1×10^5 chords were collected for every bin.

3. Results and discussion

3.1. Chord length distribution functions

To characterize the degree of heterogeneity within granular matter Aste and Di Matteo [44] determined Voronoi volume distributions (VVDs) for a variety of experimental and simulated random sphere packings. They showed that these distributions follow a so-called *k*-gamma function. In contrast to granular media VVDs are not applicable to a monolith for the lack of a building unit that defines the Voronoi centres. But considering that Voronoi volumes measure the local density of the analyzed structure, other local density measures accessible by image analysis may achieve the desired characterization as well. In recent publications it was shown that the pore space of particulate beds and monolithic silica can also be described by chord length distributions (CLDs) [32–34]. The calculation is based on a statistically significant amount of randomly generated linear paths through the interparticle or interskeleton void space of the fixed-bed structures (image background) at varying angles, providing a distribution of linear skeleton-to-skeleton distances in the case of a monolith. Fig. 2 provides an illustration of this approach. A mathematical description of the collected CLDs is achieved by fitting a simplified *k*-gamma function:

$$f(l_c) = \frac{k^k}{\Gamma(k)} \cdot \frac{l_c}{\mu_c} \cdot \exp\left(-k\frac{l_c}{\mu_c}\right) \quad (1)$$

Here, l_c denotes the chord length, μ_c is the mean chord length as a first-moment parameter of location, and k is a second-moment parameter defining the dispersion of the distribution function. For CLDs, k is defined by the mean and the standard deviation σ as:

$$k = \frac{\mu_c^2}{\sigma^2} \quad (2)$$

Since image analysis by CLDs does not require any morphological prerequisites, the adoption of this approach to monoliths becomes straightforward. An example for a *k*-gamma fit using the CLD data from Hybrid Column A4 is shown in Fig. 1C. In the following analysis, an interpretation based on the CLDs in terms of the resulting eddy dispersion and its individual contributions is provided using the obtained functional parameters μ_c and k (cf. Eq. (1) and Fig. 1C). As we will see this is an insightful and diagnostic connection because it explains the differences in the observed column efficiencies for a set of custom-prepared capillary hybrid silica monoliths.

3.2. Reproducibility

To estimate the reproducibility of the determined morphological parameters three image stacks of the highly efficient Hybrid Column A4 ($H = 4.7$ μm) were recorded at different times and positions in the detection window's volume. Table 1 illustrates the reproducibility that can be achieved using the CLD method: these values for the mode, the mean, and k differ by no more than 2%. This implies that the analyzed microscopic region is large enough to reflect the macroscopic behavior of the column. Still, an analogous determination for a more heterogeneous monolith, like the Hybrid Column B1 ($H = 8.2$ μm), will increase the scatter of the data, as illustrated in Table 2. However, the reproducibility remains good enough to allow general conclusions with this analysis about the monolith morphology.

Further, reconstructions along the whole column diameter are faced with an increased amount of signal intensity fluctuations compared to reconstructions of the bulk [32]. The main source of these fluctuations can be assigned to an increased reabsorption of the fluorescence signal (by above dye) within regions near the column centre compared to regions close to the column wall. Therefore, for a comparative study, the image processing routine was required to be reproducible and insensitive to these fluctuations. Porosity profiles for Hybrid Columns A4 and B1 are presented in Figs. 1D and 3B, respectively. Since no systematic variations following a cylindrical shape became detectable we considered the reconstructions as suitable for morphological comparisons.

3.3. Transchannel effects

Giddings has divided velocity heterogeneities into different categories that contribute to eddy dispersion in a packed bed [45]. These time and length scale classifications can also be applied to monolithic columns [46]. Our morphological analysis focuses on the transchannel, short-range interchannel, and transcolumn contributions to eddy dispersion. The long-range interchannel contribution, introduced by Giddings to account for packing heterogeneity on a length scale of about ten particle diameters in a particulate bed, will be neglected since the monoliths are not prepared through a slurry packing process [46].

The transchannel contribution to eddy dispersion arises from the lateral distribution of velocities inside each macropore (flow-through channel). It resembles the parabolic Hagen–Poiseuille flow profile in a cylinder. Thus, if we assume self-similarity for the monoliths the linear relationship between plate height and axial dispersion coefficient results in a squared dependence of column efficiency on the macropore diameter. In a well-prepared monolithic column, without strong wall effects and a relatively homogeneously reproduced monolith domain, transchannel dispersion becomes the dominant dispersion term.

Table 1
Reproducibility of morphological parameters for Hybrid Column A4 (H = 4.7 μm)[a].

	Number of images	Capillary diameter [μm]	Macropore porosity	μ_c [μm]	k	Mode [μm]
Measurement 1	155	100.8	0.697	4.96	2.39	2.89
Measurement 2	158	100.9	0.696	4.93	2.44	2.91
Measurement 3	105	100.8	0.702	4.94	2.41	2.89

[a] μ_c, k, and the mode were calculated from 1×10^6 chords fitted with a k-gamma function.

Table 2
Reproducibility of morphological parameters for Hybrid Column B1 (H = 8.2 μm)[a].

	Number of images	Column diameter [μm]	Macropore porosity	μ_c [μm]	k	Mode [μm]
Measurement 1	113	101.3	0.693	5.00	2.29	2.80
Measurement 2	139	101.2	0.688	4.92	2.31	2.85
Measurement 3	117	100.7	0.717	5.22	2.35	2.99

[a] μ_c, k, and the mode were calculated from 1×10^6 chords fitted with a k-gamma function.

Table 3
Morphological parameters and separation efficiency of the hybrid silica monoliths[a].

Column label	Column diameter [μm]	Macropore porosity	μ_c [μm]	k	Mode [μm]	H [μm]
A1	100.5	0.678	3.64	2.23	2.01	4.0
A2–C18	100.4	0.686	4.23	2.46	2.51	4.3
A3	101.2	0.680	4.61	2.35	2.65	4.6
A4	100.9	0.698	4.94	2.41	2.90	4.7
A5	98.64	0.702	5.65	2.51	3.40	6.7
A6	98.64	0.694	5.53	2.46	3.28	7.0
A7	98.58	0.692	5.62	2.51	3.39	7.0
B1	101.1	0.699	5.05	2.35	2.90	8.2
B2	98.9	0.689	4.81	2.45	2.84	8.3
B3	99.6	0.698	5.19	2.33	2.97	8.6
B4	99.9	0.698	4.51	2.38	2.61	9.6

[a] Capillaries that revealed chromatographic band broadening dominated by their macropore size according to our analysis where labeled as A1–A7, whereas columns dominated by transcolumn dispersion were labeled as B1–B4. The label "C18" identifies a C18-modified surface.

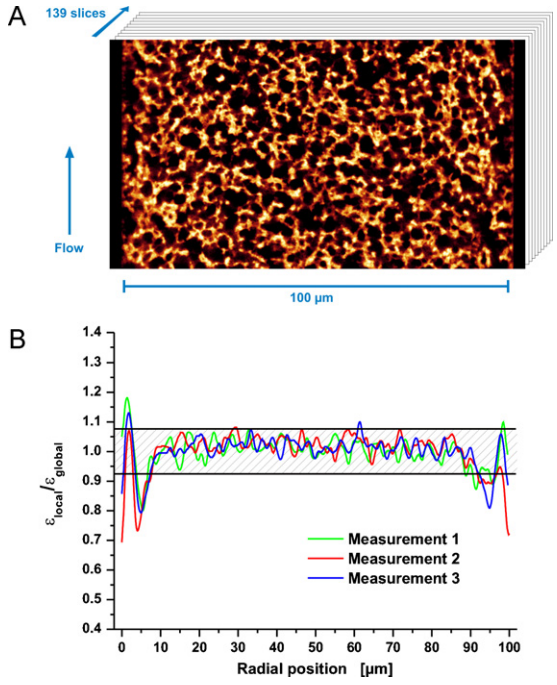

Fig. 3. Exemplary image from the second measurement of Hybrid Column B1 (A) and normalized radial porosity profiles calculated for a step size of 30 nm smoothed with a 1 μm moving window for three image stacks obtained at different times and positions in the detection window's volume of Hybrid Column B1 (B). The shading designates an area of ±1 standard deviation around the global mean porosity.

Since each derived chord is a one-dimensional measure of void distance in an analyzed image the first moment of a k-gamma fit (μ_c) directly provides a measure of the mean pore size and thus a correlation with the transchannel eddy dispersion. Alternatively, the mode of the fitted function, as the most frequent linear skeleton-to-skeleton distance, can be used to receive values that are more familiar with respect to other pore size estimates. It comprises the monolith's correlation length. Irrespective of the employed value (mode or mean), the column efficiency of the analyzed monoliths, in fact, mostly scaled with the macropore size. Results are summarized in Fig. 4A and Table 3. Hybrid Columns B1–B4 were found to deviate considerably from this anticipated behavior (red crosses in Fig. 4A). Since the mesoporosity of the monolith skeleton can be neglected for the band broadening of an unretained tracer [47], the deviations in our opinion result from a significant increase in heterogeneity on the length scale of short-range interchannel and/or transcolumn dispersion, which we consider next.

3.4. Short-range interchannel effects

The second term in eddy dispersion that we consider is the short-range interchannel contribution. Whereas transchannel dispersion on the scale of individual macropores takes place in any monolith, ordered or random, short-range heterogeneity is associated with the local disorder in real monoliths compared with perfectly ordered, crystal-like structures. For example, in random sphere packings a short-range packing heterogeneity is associated with local disorder on the scale of 1–2 particle diameters [48]. Schenker et al. [49] have shown that the parameter k in the k-gamma functions applied to the VVDs is a sensitive measure towards the degree of heterogeneity of granular packings;

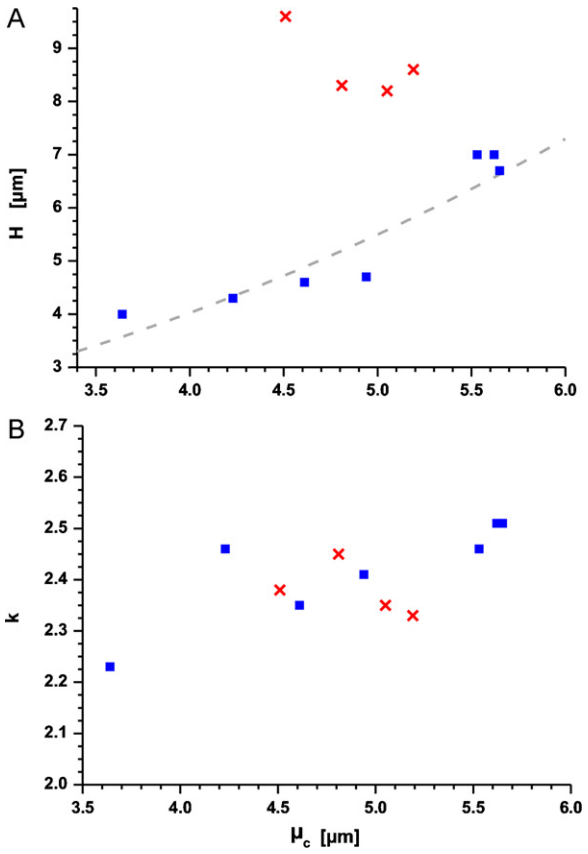

Fig. 4. Dependence of plate height (A) and k-value (B) on the mean macropore size of columns dominated by transchannel dispersion (blue squares) or transcolumn dispersion (red crosses). A quadratic dependence of H on μ_c was fitted (dashed gray line) to illustrate the anticipated dependence of column efficiency on the macropore size. (For interpretation of the references to color in this figure legend, the reader is referred to the web version of the article.)

the lower the value of k, the more heterogeneous is the structure. k is a second-moment parameter, and thus describes the variability of the pore sizes. Concurrently, the parameter k in connection with the determined CLDs (Fig. 1C) is adaptable as an expression for the overall heterogeneity of the monolithic columns.

For particle-packed beds a reduction of particle size increases separation efficiency, although this is only strictly true, if the arrangement of the particles does not change to create a more heterogeneous microstructure, i.e., if self-similarity of the packings is given. The same reasoning applies to a reduction of macropore size in monolithic columns, which has not always yielded the expected improvements in performance [13,50]. The realized degree of structural homogeneity in a monolith is a characteristic of its chemical composition, formation mechanism, and preparation conditions (similar to the slurry-packing process for particulate beds, in which case particle properties, such as shape, density, size distribution, and surface roughness, but also column dimensions, properties of the slurry liquid, and process control parameters such as the packing pressure play a role). All three aspects are very similar for the monolithic columns analyzed in this study, and we would thus expect only minor variations in heterogeneity on the length scale characteristic of short-range interchannel dispersion. With k as the measure, higher k-values express increased homogeneity of the monolith's macropore space. The generation of CLDs and corresponding calculations for the computer-generated bulk (unconfined) packings of monosized spheres of Khirevich et al. [48] at the random-close packing limit, i.e., at an interparticle porosity of 0.366, provided us with a reference point of $k = 1.97$ for particulate beds.

The analyzed hybrid monoliths generally yielded considerably higher values of $k = 2.35 \pm 0.15$ (Table 3 and Fig. 4B). Compared to Chromolith CapRod columns in our studies, which only provide a value of $k = 1.9 \pm 0.1$ over the whole column diameter (data not shown), and the densely packed particulate column in [33] with $k = 2.0$, this is a drastic increase in the structural homogeneity and underlines the enormous potential of the silica monoliths in HPLC stationary phase design. Comparing the k-values for the different hybrid columns analyzed in this work no systematic variations became evident, i.e., all columns performed similar on the length scale of short-range interchannel dispersion (see Fig. 4B). It is tempting to assign the increased homogeneity to favorable effects of the added MTMS, which should mitigate the degree of condensation during decomposition and reduce the shrinkage of the monolith. Still, a custom-prepared bare-silica TMOS monolith presented in [51] also demonstrated a k-value of 2.4 after passing through our CLD analysis, so that we have to assign the increased homogeneity to improved preparation conditions rather than to the modified material composition.

3.5. Transcolumn effects

In cases where we were not able to correlate the column efficiency of the monoliths with the mean (or mode) of their CLDs and, thus, their macropore size, the radial heterogeneity and transcolumn velocity bias, as the third eddy dispersion contribution, was found responsible. In our previous study with particulate beds the radial porosity profiles already proved to be an efficient criterion to approach this measure from image analysis [33]. The transcolumn porosity profiles in Fig. 1D can be regarded as "reference profiles" for a hybrid column with a good radial homogeneity: beyond a low-porosity wetting layer in the vicinity of the column wall the porosity profiles rapidly become almost flat and move erratically around their mean. In contrast to these good transcolumn porosity profiles for Hybrid Column A4 in Fig. 1D, the profiles for Hybrid Column B1 (Fig. 3B) show a region of increased porosity near the column wall, before after ~5 µm towards the column centre a minimum is reached and the profiles only thereafter become flat as for Hybrid Column A4. Thus, parts of Hybrid Column B1 were snapped from the column wall and the separation efficiency of the capillary is reduced due to a nearly symmetric wall effect with respect to the column axis (Fig. 3B). Hybrid Columns B2 and B4 both exhibited similar profiles as Hybrid Column B1, suffering from a ~5 µm wall gap, but only at the left column wall. Hence, for Hybrid Columns B2 and B4 the wall effect became asymmetric.

While our analysis so far has provided very consistent results reflecting properly the morphology and chromatographic performance of the individual monoliths, one inconsistency remained. Hybrid Column B3 displayed an almost flat porosity profile (Fig. 5B) and the CLD analysis gave $\mu_c = 5.2$ µm and $k = 2.3$. Consequently, we expected a better chromatographic performance than the $H = 8.6$ µm in Table 3. A closer inspection of the radial macropore size distribution provided the solution to this puzzle. Usually, the first moment of the CLDs that we calculated for these hybrid columns would vary locally in a 20%-band around its global value when plotted along radial position. This was also the case for Hybrid Columns B1 and B2, but Hybrid Column B3 demonstrated a 34% increase in the vicinity of the right column wall (Fig. 5C). We expect that this "second-kind" wall defect results from partial breakaways of the monolith's rods from the column wall, whereas the "first-kind" wall defect would appear when the majority of rods dismantle. Both effects combined could only be found in Hybrid Column B4; the worst performing column in our analysis (Table 3).

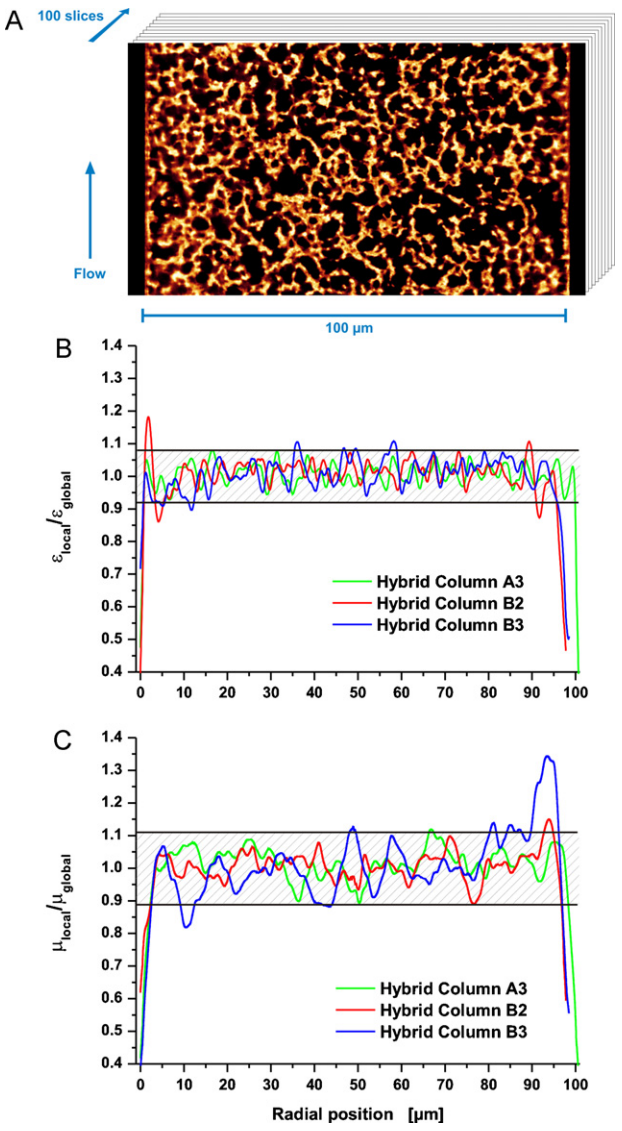

Fig. 5. Exemplary image from the 100 images recorded for Hybrid Column B3 (A). The normalized macropore porosity profile (B) and the normalized macropore size profile (C) of the stack are compared with profiles of a column dominated by transchannel dispersion (Hybrid Column A3) and a column with obvious wall gap (Hybrid Column B2). The shading designates an area of ±1 standard deviation around the global mean porosity and macropore size, respectively.

4. Conclusions

We presented an image analysis-based characterization of capillary hybrid silica monoliths. It enabled the comparison of fixed-bed heterogeneity and transport properties of these columns. Typically porosity, as a scalar parameter for column permeability, and domain size, as an equivalent to the particle diameter of particulate beds, are provided in the characterization of a monolithic column. The presented chord length analysis carries the possibility to provide a more thorough analysis of eddy dispersion contributions in a monolithic column in terms of its characteristic length scales.

CLDs for the macropore space of particulate and monolithic silica columns follow a two-parameter distribution function. The parameter of location, the arithmetic mean, provides an alternative quantitative measure for pore size which is crucial to column efficiency. The average pore size of a column correlates with transchannel dispersion, whereas the *k*-value obtained from the CLDs provides a scalar measure for column heterogeneity on the length scale of short-range interchannel dispersion.

Capillary hybrid silica monoliths prepared by a protocol described in Hara et al. [38] resulted in higher *k*-values, i.e., less variation in macropore size, than commercial Chromolith CapRod columns. Their efficiency predominantly scaled with the macropore size (its mean or mode). A further downscaling of the macropore size and simultaneously leaving the overall structural homogeneity of the material unaffected will be a challenging task, but in the present study the single most important limitation to efficient separations was the column's radial heterogeneity, i.e., the associated transcolumn velocity bias and resulting eddy dispersion. It was analyzed using the radial profiles of macropore porosity and macropore size. Whenever the separation efficiency of a column was worse than expected from its pore size, either a wall gap, cracks, or a radially nonuniform distribution of pore size was observed along the column diameter. These defects and heterogeneities were mostly of noncylindrical nature, so that the capillary diameter (as opposed to the capillary radius) takes over as the characteristic lateral equilibration length on the column scale. This, in turn, effects a much larger chromatographic band broadening.

Because any polycondensation reaction will result in a certain degree of shrinkage, in-column prepared capillary monoliths will always exhibit a stressed structure. Thus, the above limitations cannot be resolved completely. Our analysis has shown that careful preparation conditions can increase the overall structural homogeneity of a silica monolith, whereas the added MTMS may increase the rate of success in the preparation of a radially homogenous monolith. Resolving the presence of the CLSM-visualized and analyzed wall effects promises a substantial improvement in column performance. Still, according to our experience, even a readily prepared monolith might change its morphology later on due to ageing. For example, Hybrid Column B1 used to perform with an efficiency similar to that of Hybrid Column A4 from the same batch, but after remeasuring the efficiency of Hybrid Column B1 in a run-up to the present study its efficiency dropped due to a wall gap. A similar observation was made for a TMOS column presented in 2006 [51], and we expect that monolithic columns change their morphology gradually over time when persistently stressed by shrinkage.

Acknowledgements

This work was supported by the Deutsche Forschungsgemeinschaft DFG (Bonn, Germany) under grants TA 268/3-1 and TA 268/6-1. We thank Martin Kollmann and Professor Joachim Schachtner (Department of Biology, Philipps-Universität Marburg) for their help with the CLSM measurements.

References

[1] G. Guiochon, J. Chromatogr. A 1168 (2007) 101.
[2] A. Jungbauer, R. Hahn, J. Chromatogr. A 1184 (2008) 62.
[3] K.K. Unger, R. Skudas, M.M. Schulte, J. Chromatogr. A 1184 (2008) 393.
[4] H. Aoki, N. Tanaka, T. Kubo, K. Hosoya, J. Sep. Sci. 32 (2009) 341.
[5] F. Sinner, M.R. Buchmeiser, Macromolecules 33 (2000) 5777.
[6] B. Mayr, G. Hölzl, K. Eder, M.R. Buchmeiser, C.G. Huber, Anal. Chem. 74 (2002) 6080.
[7] F. Svec, J. Sep. Sci. 27 (2004) 747.
[8] K. Nakanishi, N. Tanaka, Acc. Chem. Res. 40 (2007) 863.
[9] K. Nakanishi, H. Minakuchi, N. Soga, N. Tanaka, J. Sol–Gel Sci. Technol. 8 (1997) 547.
[10] K. Nakanishi, J. Porous Mater. 4 (1997) 67.
[11] H. Minakuchi, K. Nakanishi, N. Soga, N. Ishizuka, N. Tanaka, J. Chromatogr. A 762 (1997) 135.
[12] K. Nakanishi, H. Minakuchi, N. Soga, N. Tanaka, J. Sol–Gel Sci. Technol. 13 (1998) 163.
[13] H. Minakuchi, K. Nakanishi, N. Soga, N. Ishizuka, N. Tanaka, J. Chromatogr. A 797 (1998) 121.
[14] N. Ishizuka, H. Minakuchi, K. Nakanishi, N. Soga, N. Tanaka, J. Chromatogr. A 797 (1998) 133.
[15] F. Gritti, W. Piatkowski, G. Guiochon, J. Chromatogr. A 978 (2002) 81.
[16] F.C. Leinweber, U. Tallarek, J. Chromatogr. A 1006 (2003) 207.
[17] M. Kele, G. Guiochon, J. Chromatogr. A 960 (2002) 19.

[18] U. Tallarek, F.C. Leinweber, A. Seidel-Morgenstern, Chem. Eng. Technol. 25 (2002) 1177.
[19] F. Gritti, W. Piatkowski, G. Guiochon, J. Chromatogr. A 983 (2003) 51.
[20] K. Cabrera, J. Sep. Sci. 27 (2004) 843.
[21] J.R. Mazzeo, U.D. Neue, M. Kele, R.S. Plumb, Anal. Chem. 77 (2005) 460A.
[22] R.T. Kennedy, J.W. Jorgenson, Anal. Chem. 61 (1989) 1128.
[23] G. Guiochon, E. Drumm, D. Cherrak, J. Chromatogr. A 835 (1999) 41.
[24] R.A. Shalliker, B.S. Broyles, G. Guiochon, J. Chromatogr. A 888 (2000) 1.
[25] R.A. Shalliker, V. Wong, B.S. Broyles, G. Guiochon, J. Chromatogr. A 977 (2002) 213.
[26] R.S. Maier, D.M. Kroll, R.S. Bernard, S.E. Howington, J.F. Peters, H.T. Davis, Phys. Fluids 15 (2003) 3795.
[27] S. Khirevich, A. Höltzel, D. Hlushkou, U. Tallarek, Anal. Chem. 79 (2007) 9340.
[28] S. Khirevich, A. Höltzel, A. Seidel-Morgenstern, U. Tallarek, Anal. Chem. 81 (2009) 7057.
[29] J.A. Abia, K.S. Mriziq, G.A. Guiochon, J. Chromatogr. A 1216 (2009) 3185.
[30] J.A. Abia, K.S. Mriziq, G.A. Guiochon, J. Sep. Sci. 32 (2009) 923.
[31] N. Ishizuka, H. Kobayashi, H. Minakuchi, K. Nakanishi, K. Hirao, K. Hosoya, T. Ikegami, N. Tanaka, J. Chromatogr. A 960 (2002) 85.
[32] S. Bruns, T. Müllner, M. Kollmann, J. Schachtner, A. Höltzel, U. Tallarek, Anal. Chem. 82 (2010) 6569.
[33] S. Bruns, U. Tallarek, J. Chromatogr. A 1218 (2011) 1849.
[34] J. Courtois, M. Szumski, F. Georgsson, K. Irgum, Anal. Chem. 79 (2007) 335.
[35] D. Hlushkou, S. Bruns, U. Tallarek, J. Chromatogr. A 1217 (2010) 3674.
[36] D. Hlushkou, S. Bruns, A. Höltzel, U. Tallarek, Anal. Chem. 82 (2010) 7150.
[37] R. Roux, M. Abi Jaoudé, C. Demesmay, J. Chromatogr. A 1216 (2009) 3857.
[38] T. Hara, S. Makino, Y. Watanabe, T. Ikegami, K. Cabrera, B. Smarsly, N. Tanaka, J. Chromatogr. A 1217 (2010) 89.
[39] K. Kanamori, H. Yonezawa, K. Nakanishi, K. Hirao, H. Jinnai, J. Sep. Sci. 27 (2004) 874.
[40] M. Motokawa, M. Ohira, H. Minakuchi, K. Nakanishi, N. Tanaka, J. Sep. Sci. 29 (2006) 2471.
[41] I.H. Malitson, J. Opt. Soc. Am. 55 (1965) 1205.
[42] W.S. Rasband, ImageJ, U.S. National Institutes of Health, Bethesda, MD, 1997–2006, http://rsb.info.nih.gov//ij/.
[43] S. Bochkanov, V. Bystritsky, ALGLIB (www.alglib.net).
[44] T. Aste, T. Di Matteo, Phys. Rev. E 77 (2008) 021309.
[45] J.C. Giddings, Dynamics of Chromatography. Part 1: Principles and Theory, Marcel Dekker, New York, 1965.
[46] F. Gritti, G. Guiochon, J. Chromatogr. A 1216 (2009) 4752.
[47] D. Hlushkou, S. Bruns, A. Seidel-Morgenstern, U. Tallarek, J. Sep. Sci. 34 (2011) in press, doi:10.1002/jssc.201100158.
[48] S. Khirevich, A. Daneyko, A. Höltzel, A. Seidel-Morgenstern, U. Tallarek, J. Chromatogr. A 1217 (2010) 4713.
[49] I. Schenker, F.T. Filser, L.J. Gauckler, T. Aste, H.J. Herrmann, Phys. Rev. E 80 (2009) 021302.
[50] H. Kobayashi, D. Tokuda, J. Ichimaru, T. Ikegami, K. Miyabe, N. Tanaka, J. Chromatogr. A 1109 (2006) 2.
[51] T. Hara, H. Kobayashi, T. Ikegami, K. Nakanishi, N. Tanaka, Anal. Chem. 78 (2006) 7632.